Supporting Information

Resonant coupling of moiré exciton to phonon in a WSe$_2$/MoSe$_2$ heterobilayer

Keisuke Shinokita[1]*, Yuhei Miyauchi[1], Kenji Watanabe[2], Takashi Taniguchi[3], Kazunari Matsuda[1]*

[1]Institute of Advanced Energy, Kyoto University, Uji, Kyoto 611-0011, Japan

[2]Research Center for Functional Materials, National Institute for Materials Science, 1-1 Namiki, Tsukuba, Ibaraki 305-0044, Japan

[3]International Center for Materials Nanoarchitectonics, National Institute for Materials Science, 1-1 Namiki, Tsukuba, Ibaraki 305-0044, Japan

*Corresponding authors: shinokita.keisuke.4r@kyoto-u.ac.jp, matsuda@iae.kyoto-u.ac.jp

Section S1. Determination of stacking angle

A second harmonic generation (SHG) measurement was performed to determine the stacking angle of the twisted MoSe$_2$/WSe$_2$ heterobilayer. A linearly polarized femtosecond laser pulse (80 MHz, 900 nm, ~100 fs) was focused onto the MoSe$_2$/WSe$_2$ heterobilayer and a MoSe$_2$ monolayer sample with a 100× objective lens. The SHG signal at 450 nm with cross-polarized components was collected using the same objective lens and detected with a CCD coupled with a spectrometer. The angle dependence of the SHG signal was measured by rotating the laser polarization with a half-wave plate. Under this condition, the SHG signal has maximum values when the laser polarization is parallel to the zigzag directions of monolayer semiconducting transition metal dichalcogenides (TMDs)[1].

Figure S1 shows the angle dependence of the SHG signals of the MoSe$_2$ monolayer and MoSe$_2$/WSe$_2$ heterobilayer. The solid lines are results fitted with $\cos^2(3\theta)$, where θ is the relative angle between the laboratory and crystalline coordinates. While both the MoSe$_2$ monolayer and MoSe$_2$/WSe$_2$ heterobilayer show sixfold symmetry reflecting the crystal symmetry, the peak angles are different, and their difference is evaluated as ~6°. Because the SHG signal of the heterobilayer has a maximum between the MoSe$_2$ and WSe$_2$ monolayer maximum angles, the stacking angle of MoSe$_2$ and WSe$_2$ is determined to be ~12±1°. The SHG signal from the heterobilayer is stronger than that from the MoSe$_2$ monolayer (constructive interference), suggesting that the stacking of the heterobilayer is R-type (close to 0°) rather than H-type (close to 60°). In addition, the circularly-polarized PL spectra could be used to determine the stacking, because the circularly-polarized PL spectra show different behavior in circularly-polarization with R- and H-type stacking originating from different band alignment[2]. In the case of R-type stacking,

the cross-circular polarized emission signal is stronger than the co-circular polarized emission under the circularly-polarized excitation, which is consistent with the results in this study (Fig. S9).
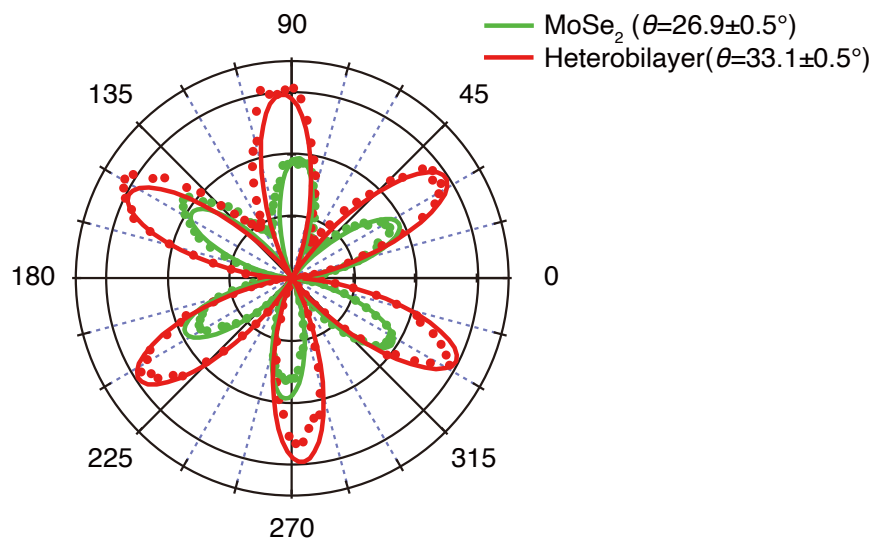

Figure S1. Determination of the MoSe$_2$/WSe$_2$ twist angle by polarization-resolved SHG measurement. The sixfold symmetry in the SHG intensity (points) and fits (solid lines) for the MoSe$_2$ monolayer (green) and the MoSe$_2$/WSe$_2$ heterobilayer (red).

Section S2. Raman scattering spectra

Raman scattering spectra were measured with a micro-PL setup with a 2.33 eV semiconductor laser at room temperature. Figure S2 shows the Raman spectra of the MoSe$_2$ monolayer and MoSe$_2$/WSe$_2$ heterobilayer. A$_1$' phonon mode of MoSe$_2$ at ~243 cm^{-1} and A$_1$'+E' phonon modes of WSe$_2$ at ~250 cm^{-1} were observed. Here we use single-layer notation for the Raman modes. The Raman scattering spectrum of the heterobilayer is described with the simple sum of the A$_1$' phonon

3

mode of $MoSe_2$ and $A_1'+E'$ phonon modes of WSe_2, which suggest the phonon modes are not affected by the softening and the broadening due to the moiré potential. These are consistent with the previously reported results[3,4].
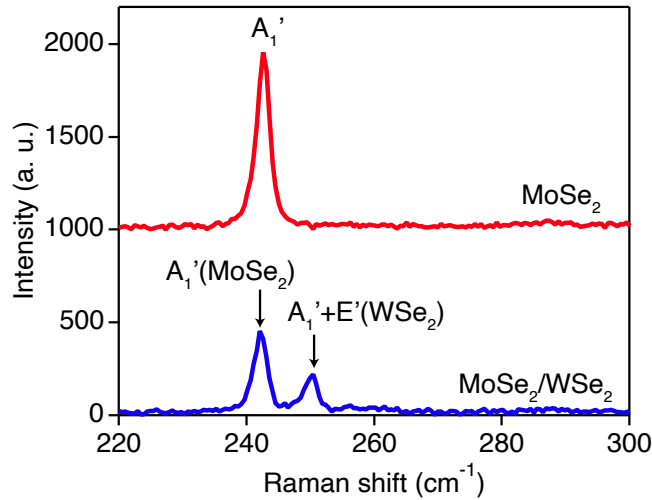

Figure S2. Raman scattering spectra of the $MoSe_2$ monolayer and $MoSe_2/WSe_2$ heterobilayer under 2.33-eV laser excitation.

Section S3. Estimation of the temperature increase

To evaluate the heating effect in the power dependence of the PL spectrum (Fig. 3), we estimated the temperature increase under laser irradiation. Based on the specific heat of 0.278 $Jg^{-1}K^{-1}$ and density of 6.96 g/cm^3, the temperature increase under the photoexcitation laser (photon energy of 1.55 eV) with a maximum intensity of 10^6 W/cm^2 is only ΔT_{max}=12 $K^{5,6}$. By considering the temperature-dependent redshift of 0.317 meV/K^7 and constant linewidth below 50 K in monolayer $TMDs^8$, we concluded that the increase in temperature is not significant in the measurement.

Section S4. Estimation of the exciton density and PL lifetime

We measured the PL intensity under pulsed and continuous wave (cw) excitation to estimate the generated exciton density. As shown in Fig. S3, the PL intensity reflecting the bright exciton density is almost identical under both cw and pulsed excitation. Therefore, we evaluated the excited exciton density under cw excitation based on the experimental results under pulsed excitation. The incident photon number under pulsed excitation is described as $N_{ph} = (1-R)\alpha dP\tau_{rep}/\hbar\omega$. The excited exciton density can be calculated with $N_{ex} = (1-R)\alpha dP\tau_{rep}/\hbar\omega$. Here, R is the reflectivity, α is the absorption coefficient, d=0.7 nm is the thickness of the monolayer, P is the power density, τ_{rep}=12 ns is the laser repetition rate, and $\hbar\omega$=1.55 eV is the photon energy.

On the other hand, under cw excitation with exciton generation rate g, the excited exciton density in the steady state is calculated by considering the following rate equation using non-radiative and radiative recombination times τ_{nrad} and τ_{rad}, respectively.

$$\frac{dN_{ex}}{dt} = g - \frac{N_{ex}}{\tau_{nrad}} - \frac{N_{ex}}{\tau_{rad}}. \tag{S1}$$

In the steady state condition,

$$N_{ex} = \left(\frac{1}{\tau_{nrad}} + \frac{1}{\tau_{rad}}\right)^{-1} \times g. \tag{S2}$$

Because the exciton generation rate is given by $g = (1-R)\alpha dP/\hbar\omega$, the excited exciton density is $\left(\frac{1}{\tau_{nrad}} + \frac{1}{\tau_{rad}}\right)^{-1}(1-R)\alpha dP/\hbar\omega$. As shown in Fig. S3, because the PL intensity is almost

identical under both cw and pulsed excitation, the excited exciton density is also same. As a result, we can obtain the following relationship:

$$\tau_{\text{rep}} = \left(\frac{1}{\tau_{\text{nrad}}} + \frac{1}{\tau_{\text{rad}}}\right)^{-1}. \tag{S3}$$

Therefore, the PL decay time given by $\left(\frac{1}{\tau_{nrad}} + \frac{1}{\tau_{rad}}\right)^{-1}$ is close to the laser repetition rate $\tau_{\text{rep}}=12$ ns in the sample used here.
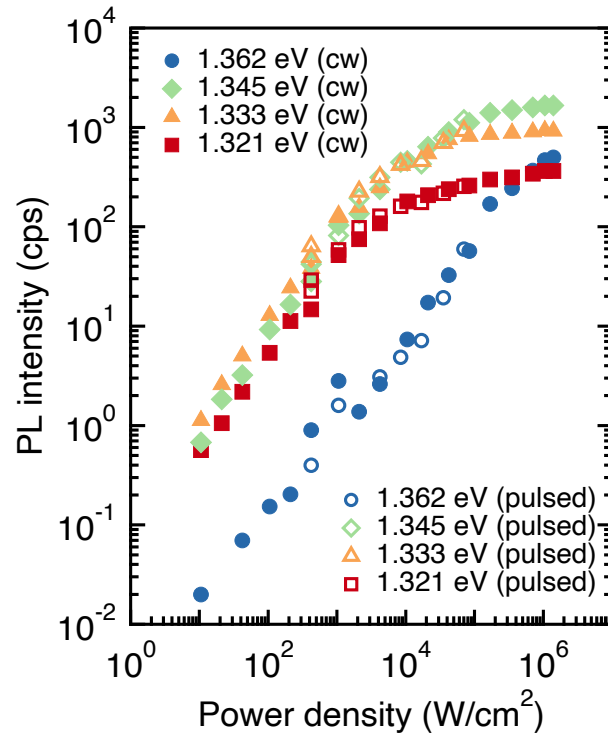

Figure S3. PL intensity as a function of excitation power density at different probe energies under cw and pulsed excitation with a photon energy of 1.55 eV.

Section S5. Fitting of PL spectra with multiple Lorentz functions

In order to evaluate the resonance energy from the PLE spectrum in Fig. 2 quantitatively, we fitted the PL spectrum with different excitation energies in Fig. S4 with twelve Lorentz functions with a linewidth of 3 meV. We selected the approximate peak energies of the Lorentz functions by consideration of emergent peaks depending the excitation energies, fitted globally all spectra with the same set of parameters, and determined the energies of Lorentz functions. The fitting results are shown in Fig. S4. The PLE spectra of each Lorentz function after the fitting as a function of excess energy are shown in Fig. S5.
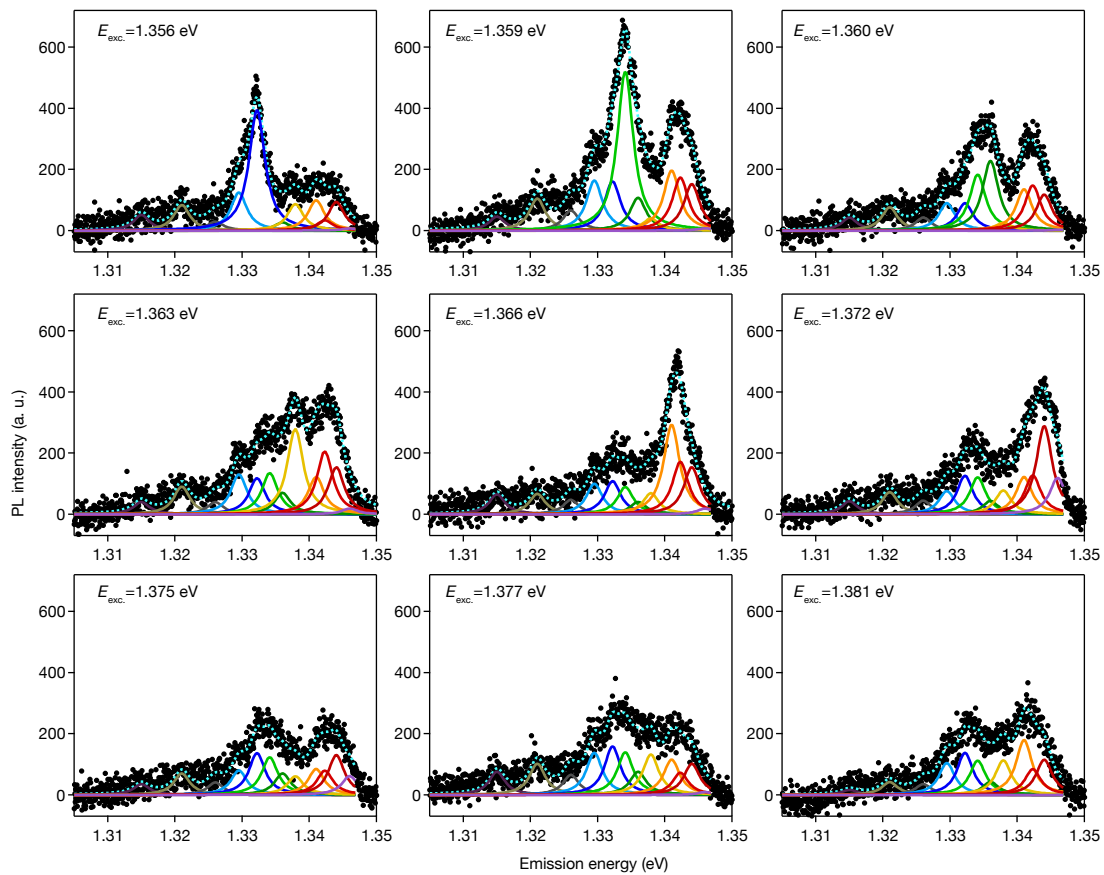

Figure S4. Results of fitting PL spectra with multiple Lorentz functions. The black circles are experimental data with different excitation energies, and the dotted cyan curves are the sum of all

peaks. The dark purple, ivory, grey, sky blue, blue, green, dark green, yellow, orange, red, dark red, and purple colours correspond to Lorentz functions with peak energies of 1.315, 1.321, 1.326, 1.330, 1.332, 1.334, 1.336, 1.338, 1.341, 1.342, 1.344, and 1.346 eV, respectively.
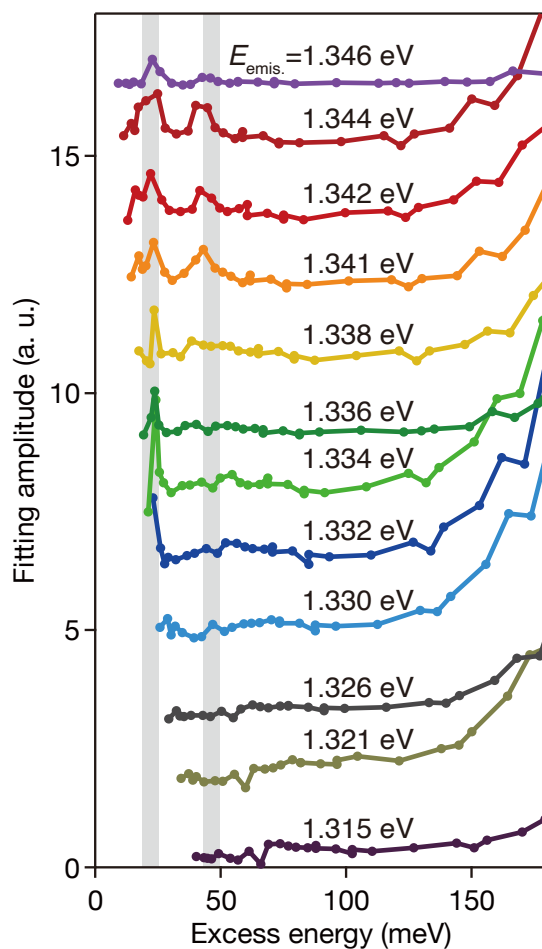

Figure S5. PLE spectrum after Lorentzian fitting of the PL spectrum as a function of excess energy. The grey filled areas show excess energies of 24 and 48 meV. The dark purple, ivory, grey, sky blue, blue, green, dark green, yellow, orange, red, dark red, and purple colours correspond to

PLE spectrum with peak energies of 1.315, 1.321, 1.326, 1.330, 1.332, 1.334, 1.336, 1.338, 1.341, 1.342, 1.344, and 1.346 eV, respectively.

Section S6. Moiré exciton energy levels

We considered a simple model to calculate the energy levels of the moiré exciton in a parabolic potential trap with depth U, moiré period $a_{\text{moiré}}$=2 nm, and exciton effective mass m=0.25m_0, resulting in an interlevel spacing of $\Delta\hbar\omega = \hbar/a_{\text{moiré}}\sqrt{2U/m}$ in the harmonic-like potential[9]. In previous reports, the moiré potential depth U was calculated to be approximately a few hundred meV in R-type stacking[10–13], and scanning tunnelling microscopy and spectroscopy (STM-STS) revealed a deep potential of a few hundred meV[14–16], which supports the observed onset of the PLE signal at approximately 150 meV in Fig. 2c and the PLE tail in Fig. 1a reflecting the continuum state of the moiré exciton (n=∞), where n is the quantum number. By assuming a moiré potential depth of U~200-300 meV, the interlevel spacing is estimated as $\Delta\hbar\omega$~160-200 meV, which is much larger than the observed energy differences of resonance peaks of 24 and 48 meV. In addition, by considering a zero-point energy $\Delta\hbar\omega/2$ in the parabolic potential, the excited states (n=2, 3, …) are outside the potential, and only the ground state of the moiré exciton (n=1) is confined in the moiré potential. This estimation is consistent with the more sophisticated first-principles-based exciton moiré potential calculated with the plane-wave expansion method, which

reports that the excited states (n=2, 3, …) are allowed only in heterobilayers with a very small twist angle of a few degrees[13].

Section S7. Simulation procedure

We numerically simulated the PL spectra under different exciton densities (Fig. 3f, g). We assumed a Gaussian distribution of energy levels with the same peak energies of Lorentz functions used in the fitting procedure of the PLE spectrum (Fig. S4) in addition with higher energy peaks conjectured from the PL spectrum at high excitation density (Fig. 3a). Then, we performed Monte Carlo simulations to evaluate how the excited excitons occupy the energy levels. In the simulation, we took into the consideration the relaxation process of the moiré exciton between different potential minima. If the energy separation between the initial and final energy level for moiré exciton relaxation is equal to the phonon energy of ~24 meV, the relaxation to the lower energy level is allowed, meaning the relaxation process is faster than the PL lifetime of ~10 ns. On the other hand, if the energy separation is not matched to the phonon energy, the relaxation to the lower energy level is forbidden because of suppressed phonon scattering. In addition, we also considered the state filling effect due to Pauli blocking: Even if the relaxation is allowed, if the final energy level is already occupied by generated excitons, the relaxation is forbidden. The state filling effect is important at high excitation density. We performed Monte Carlo simulations and simulated spectra using the linewidth extracted from the experimental data, as shown in Fig. 3f. The simulated spectra well reproduce the behaviour of the experimentally observed PL spectra in Fig. 3a: the nearly invariant spectral shape at low exciton density and the shift of the spectral median to the higher energy side at higher exciton density.

In order to test the validity of our assumption, we also simulated the opposite case that the phonon scattering is *not* suppressed and *all* relaxation to lower energy level is faster than the PL lifetime. Figure S6 shows the simulated spectra for different exciton densities, which shows different spectral shapes under various excitation power conditions in comparison with the experimentally obtained results in Fig. 3f, g: only one peak with the lowest energy is expected at a low excitation power because of the fast relaxation process to the potential minimum with the lowest energy, and as the excitation power increases, new peaks would appear beginning with the lowest energy levels because of the finite density of states and state filling effect. This behaviour could not explain the experimental observation of several peaks with invariant spectral shapes at low excitation power in Fig. 3a. Therefore, we consider the relaxation process of the moiré exciton is affected by the phonon scattering process.
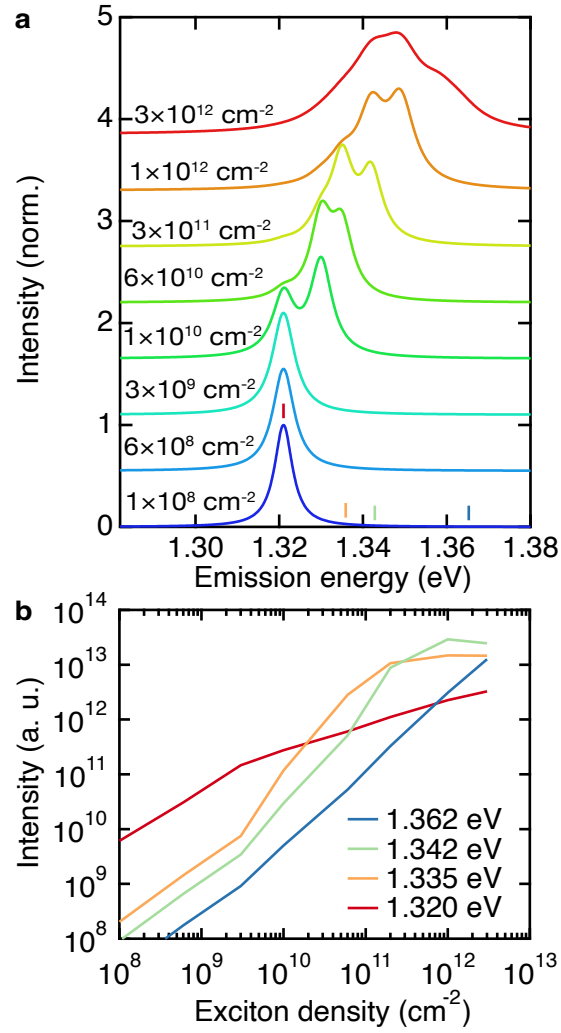
Figure S6. Simulation results in the opposite case with the unsuppressed phonon scattering. (a) Simulated spectra for different exciton densities and (b) simulated intensities as a function of exciton density assuming that *all* relaxation processes between the moiré potential minima are much faster than the PL lifetime.
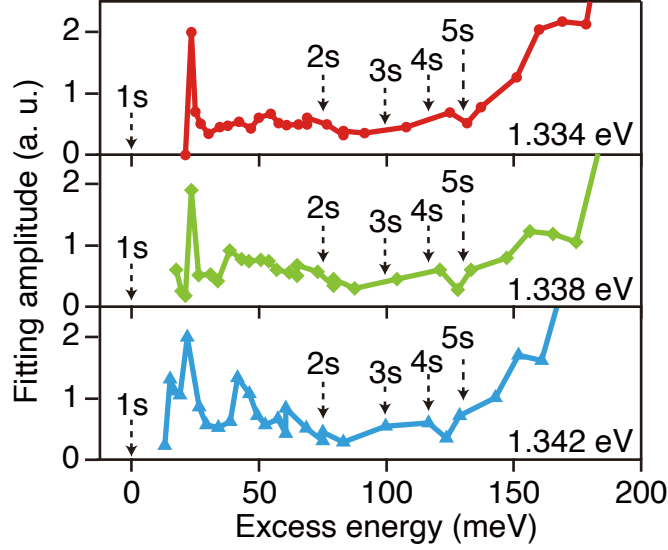
Figure S7. Comparison with excitonic Rydberg series in the non-hydrogenic 2D potential. PLE spectrum after Lorentzian fitting of the PL spectrum as a function of excess energy. The vertical axis shows the estimated Rydberg exciton series in the non-hydrogenic 2D potential assuming that the continuum state is 150 meV above the 1s ground state. The absence of the excited states of the moiré exciton is in contrast to the 2D intralayer exciton system, where the resonance signals of the excitonic Rydberg series of 2*s*, 3*s*, … are prominent in the PLE spectrum[17–19]. In the moiré system, the confinement by the in-plane moiré potential makes modification of the Rydberg excitons in the non-hydrogenic 2D potential[10]. Indeed, no prominent resonance features were observed at the estimated Rydberg energy in the non-hydrogenic 2D potential, which suggests that the moiré superlattice works as an in-plane potential and confines the interlayer exciton, causing a modification in the exciton energy level structure.
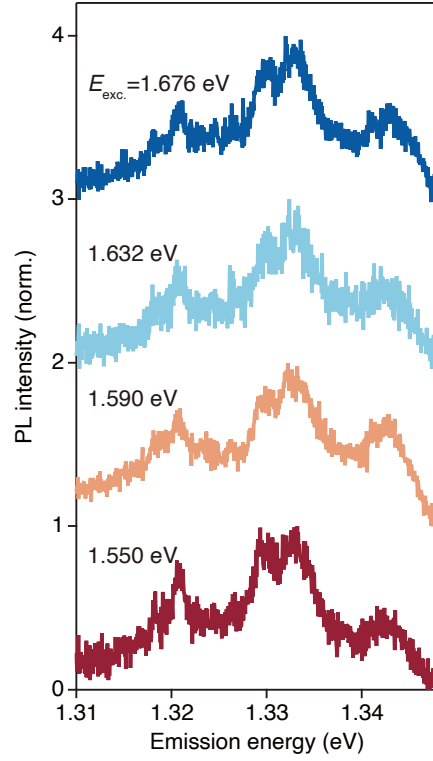
Figure S8. PL spectrum at off-resonant excitation condition above 1.4 eV. No clear differences were observed unlike that at near-resonant excitation condition below 1.4 eV, as shown in Fig. S4.
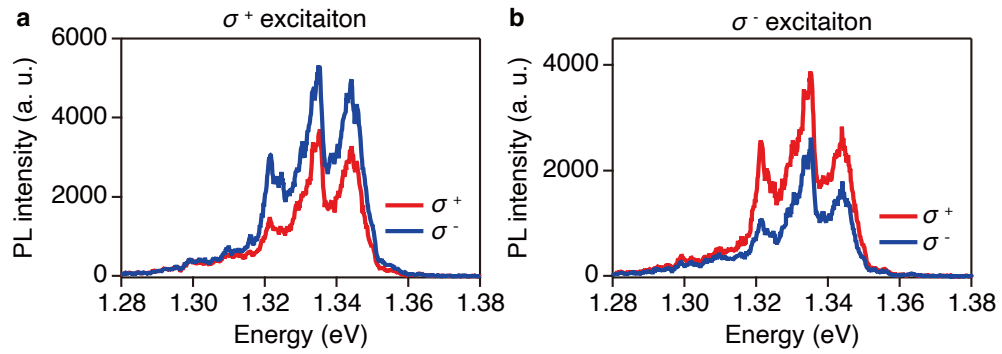

Figure S9. Circular-polarization-resolved PL spectra under (a) σ^+ and (b) σ^- excitation with photon energy of 1.7 eV at 10 K. The red and blue curves indicate σ^+ and σ^- polarized PL components, respectively.
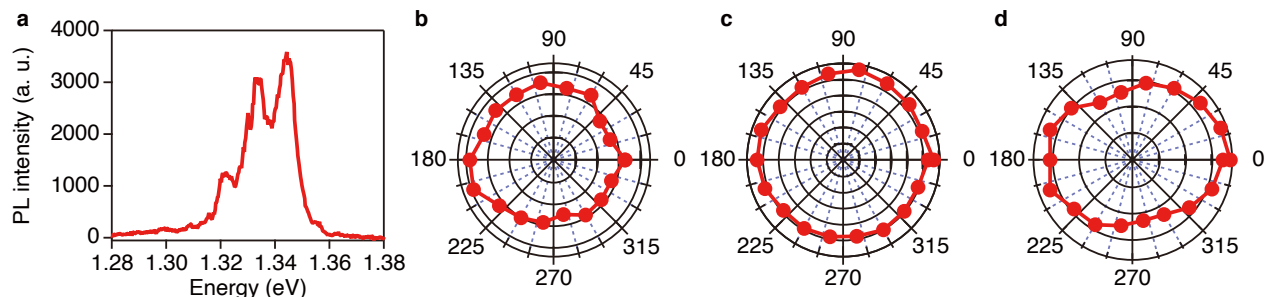
Figure S10. (a) PL spectra under linearly-polarized 1.7-eV laser excitation at 10 K. Corresponding angular dependence of the PL emission at (b) 1.324, (c) 1.333, and (d) 1.344 eV.

References

(1)   Kumar, N.; Najmaei, S.; Cui, Q.; Ceballos, F.; Ajayan, P. M.; Lou, J.; Zhao, H. Second Harmonic Microscopy of Monolayer MoS$_2$. *Phys. Rev. B* **2013**, *87*, 161403-1-161403–161406. https://doi.org/10.1103/PhysRevB.87.161403.

(2)   Seyler, K. L.; Rivera, P.; Yu, H.; Wilson, N. P.; Ray, E. L.; Mandrus, D. G.; Yan, J.; Yao, W.; Xu, X. Signatures of Moiré-Trapped Valley Excitons in MoSe$_2$/WSe$_2$ Heterobilayers. *Nature* **2019**, *567*, 66–70. https://doi.org/10.1038/s41586-019-0957-1.

(3)   Lin, M. L.; Tan, Q. H.; Wu, J. Bin; Chen, X. S.; Wang, J. H.; Pan, Y. H.; Zhang, X.; Cong, X.; Zhang, J.; Ji, W.; et al. Moiré Phonons in Twisted Bilayer MoS$_2$. *ACS Nano* **2018**, *12*, 8770–8780. https://doi.org/10.1021/acsnano.8b05006.

(4)   Nayak, P. K.; Horbatenko, Y.; Ahn, S.; Kim, G.; Lee, J. U.; Ma, K. Y.; Jang, A. R.; Lim, H.; Kim, D.; Ryu, S.; et al. Probing Evolution of Twist-Angle-Dependent Interlayer Excitons in MoSe$_2$/WSe$_2$ van Der Waals Heterostructures. *ACS Nano* **2017**, *11*, 4041–4050. https://doi.org/10.1021/acsnano.7b00640.

(5)   Kiwia, H. L.; Westrum, E. F. Low-Temperature Heat Capacities of Molybdenum Diselenide and Ditelluride. *J. Chem. Thermodyn.* **1975**, *7*, 683–691. https://doi.org/10.1016/0021-9614(75)90009-9.

(6) Lin, M. F.; Kochat, V.; Krishnamoorthy, A.; Bassman, L.; Weninger, C.; Zheng, Q.; Zhang, X.; Apte, A.; Tiwary, C. S.; Shen, X.; et al. Ultrafast Non-Radiative Dynamics of Atomically Thin $MoSe_2$. *Nat. Commun.* **2017**, *8*, 1745. https://doi.org/10.1038/s41467-017-01844-2.

(7) Yu, Y.; Bataller, A. W.; Younts, R.; Yu, Y.; Li, G.; Puretzky, A. A.; Geohegan, D. B.; Gundogdu, K.; Cao, L. Room Temperature Electron-Hole Liquid in Monolayer MoS_2. *ACS Nano* **2019**, *13*, 10351–10358. https://doi.org/10.1021/acsnano.9b04124.

(8) Shinokita, K.; Wang, X.; Miyauchi, Y.; Watanabe, K.; Taniguchi, T.; Matsuda, K. Continuous Control and Enhancement of Excitonic Valley Polarization in Monolayer WSe_2 by Electrostatic Doping. *Adv. Funct. Mater.* **2019**, *29*, 1900260. https://doi.org/10.1002/adfm.201900260.

(9) Raynaud, C.; Claude, T.; Borel, A.; Amara, M. R.; Graf, A.; Zaumseil, J.; Lauret, J. S.; Chassagneux, Y.; Voisin, C. Superlocalization of Excitons in Carbon Nanotubes at Cryogenic Temperature. *Nano Lett.* **2019**, *19*, 7210–7216. https://doi.org/10.1021/acs.nanolett.9b02816.

(10) Yu, H.; Liu, G. Bin; Tang, J.; Xu, X.; Yao, W. Moiré Excitons: From Programmable Quantum Emitter Arrays to Spin-Orbit–Coupled Artificial Lattices. *Sci. Adv.* **2017**, *3*, e1701696. https://doi.org/10.1126/sciadv.1701696.

(11) Tran, K.; Moody, G.; Wu, F.; Lu, X.; Choi, J.; Kim, K.; Rai, A.; Sanchez, D. A.; Quan, J.; Singh, A.; et al. Evidence for Moiré Excitons in van Der Waals Heterostructures. *Nature* **2019**, *567*, 71–75. https://doi.org/10.1038/s41586-019-0975-z.

(12) Lu, X.; Li, X.; Yang, L. Modulated Interlayer Exciton Properties in a Two-Dimensional Moiré Crystal. *Phys. Rev. B* **2019**, *100*, 155416. https://doi.org/10.1103/PhysRevB.100.155416.

(13) Li, Z.; Lu, X.; Cordovilla Leon, D. F.; Lyu, Z.; Xie, H.; Hou, J.; Lu, Y.; Guo, X.; Kaczmarek, A.; Taniguchi, T.; et al. Interlayer Exciton Transport in $MoSe_2/WSe_2$ Heterostructures. *ACS Nano* **2021**, *15*, 1539–1547. https://doi.org/10.1021/acsnano.0c08981.

(14) Pan, Y.; Fölsch, S.; Nie, Y.; Waters, D.; Lin, Y. C.; Jariwala, B.; Zhang, K.; Cho, K.; Robinson, J. A.; Feenstra, R. M. Quantum-Confined Electronic States Arising from the Moiré Pattern of MoS_2-WSe_2 Heterobilayers. *Nano Lett.* **2018**, *18*, 1849–1855.

https://doi.org/10.1021/acs.nanolett.7b05125.

(15) Li, H.; Li, S.; Naik, M. H.; Xie, J.; Li, X.; Wang, J.; Regan, E.; Wang, D.; Zhao, W.; Zhao, S.; et al. Imaging Moiré Flat Bands in Three-Dimensional Reconstructed WSe_2/WS_2 Superlattices. *Nat. Mater.* **2021**. https://doi.org/10.1038/s41563-021-00923-6.

(16) Shabani, S.; Halbertal, D.; Wu, W.; Chen, M.; Liu, S.; Hone, J.; Yao, W.; Basov, D. N.; Zhu, X.; Pasupathy, A. N. Deep Moiré Potentials in Twisted Transition Metal Dichalcogenide Bilayers. *Nat. Phys.* **2021**. https://doi.org/10.1038/s41567-021-01174-7.

(17) Hill, H. M.; Rigosi, A. F.; Roquelet, C.; Chernikov, A.; Berkelbach, T. C.; Reichman, D. R.; Hybertsen, M. S.; Brus, L. E.; Heinz, T. F. Observation of Excitonic Rydberg States in Monolayer MoS_2 and WS_2 by Photoluminescence Excitation Spectroscopy. *Nano Lett.* **2015**, *15*, 2992–2997. https://doi.org/10.1021/nl504868p.

(18) Wang, G.; Marie, X.; Gerber, I.; Amand, T.; Lagarde, D.; Bouet, L.; Vidal, M.; Balocchi, A.; Urbaszek, B. Giant Enhancement of the Optical Second-Harmonic Emission of WSe_2 Monolayers by Laser Excitation at Exciton Resonances. *Phys. Rev. Lett.* **2015**, *114*, 097403. https://doi.org/10.1103/PhysRevLett.114.097403.

(19) Tonndorf, P.; Schmidt, R.; Schneider, R.; Kern, J.; Buscema, M.; Steele, G. A.; Castellanos-Gomez, A.; van der Zant, H. S. J.; Michaelis de Vasconcellos, S.; Bratschitsch, R. Single-Photon Emission from Localized Excitons in an Atomically Thin Semiconductor. *Optica* **2015**, *2*, 347. https://doi.org/10.1364/optica.2.000347.